

<https://helda.helsinki.fi>

Physical Characterization of 2015 JD(1) : A Possibly Inhomogeneous Near-Earth Asteroid

Lopez-Oquendo, Andy

2022-08-01

Lopez-Oquendo , A , Trilling , D E , Gustafsson , A , Virkki , A , Rivera-Valentin , E G , Granvik , M , Chandler , C O , Chatelain , J , Taylor , P & Fernanda-Zambrano , L 2022 , ' Physical Characterization of 2015 JD(1) : A Possibly Inhomogeneous Near-Earth Asteroid ' , Planetary Science Journal , vol. 3 , no. 8 , 189 . <https://doi.org/10.3847/PSJ/ac7e4f>

<http://hdl.handle.net/10138/354655>

<https://doi.org/10.3847/PSJ/ac7e4f>

cc_by

publishedVersion

Downloaded from Helda, University of Helsinki institutional repository.

This is an electronic reprint of the original article.

This reprint may differ from the original in pagination and typographic detail.

Please cite the original version.



Physical Characterization of 2015 JD₁: A Possibly Inhomogeneous Near-Earth Asteroid

Andy López-Oquendo¹ , David E. Trilling¹ , Annika Gustafsson^{1,2} , Anne Virkki^{3,4} , Edgard G. Rivera-Valentín⁵ , Mikael Granvik^{4,6} , Colin Orion Chandler¹ , Joseph Chatelain⁷ , Patrick Taylor⁵ , and Luisa Fernanda-Zambrano³

¹Department of Astronomy and Planetary Science, Northern Arizona University, Flagstaff, AZ 86011, USA; al2987@nau.edu

²Southwest Research Institute, Boulder, CO 80302, USA

³Arecibo Observatory, University of Central Florida, Arecibo, PR 00612, USA

⁴Department of Physics, P.O. Box 64, FI-00014, University of Helsinki, Finland

⁵Lunar and Planetary Institute, Universities Space Research Association, Houston, TX 77058, USA

⁶Asteroid Engineering Lab, Luleå University of Technology, Box 848, SE-981 28 Kiruna, Sweden

⁷Las Cumbres Observatory, 6740 Cortona Drive, Suite 102, Goleta, CA 93117, USA

Received 2021 September 21; revised 2022 May 27; accepted 2022 June 14; published 2022 August 9

Abstract

The surfaces of airless bodies such as asteroids are exposed to many phenomena that can alter their physical properties. Bennu, the target of the OSIRIS-REx mission, has demonstrated how complex the surface of a small body can be. In 2019 November, the potentially hazardous asteroid 2015 JD₁ experienced a close approach of 0.033 1 au from the Earth. We present results of the physical characterization of 2015 JD₁ based on ground-based radar, spectroscopy, and photometric observations acquired during 2019 November. Radar polarimetry measurements from the Arecibo Observatory indicate a morphologically complex surface. The delay-Doppler images reveal a contact binary asteroid with an estimated visible extent of ~ 150 m. Our observations suggest that 2015 JD₁ is an E-type asteroid with a surface composition similar to aubrites, a class of differentiated enstatite meteorites. The dynamical properties of 2015 JD₁ suggest that it came from the ν_6 resonance with Jupiter, and spectral comparison with major E-type bodies suggests that it may have been derived from a parental body similar to the progenitor of the E-type (64) Angelina. Significantly, we find rotational spectral variation across the surface of 2015 JD₁ from the red to blue spectral slope. Our compositional analysis suggests that the spectral slope variation could be due to the lack of iron and sulfides in one area of the surface of 2015 JD₁ and/or differences in grain sizes.

Unified Astronomy Thesaurus concepts: [Asteroid surfaces \(2209\)](#); [Near-Earth objects \(1092\)](#); [Asteroids \(72\)](#); [Spectroscopy \(1558\)](#); [Photometry \(1234\)](#); [Radar astronomy \(1329\)](#)

Supporting material: data behind figures

1. Introduction

Small rocky bodies in the solar system are a type of planetary library; they have existed since planetary formation, undergoing minor geochemical alterations and recording information on processes that occurred ever since. Comprehending the nature (i.e., physical and dynamical properties) of small objects in the solar system has been of vital importance to understand their formation and evolution (Bottke et al. 2002; DeMeo & Carry 2014; Granvik et al. 2018; Binzel et al. 2019).

Wide-area asteroid surveys (i.e., the Near-Earth Object Wide-field Infrared Survey Explorer, Mainzer et al. 2011; the Panoramic Survey Telescope and Rapid Response System, Pan-STARRS, Chambers et al. 2016; Spacewatch, Rabinowitz 1991; Lincoln Near-Earth Asteroid Research, Stokes et al. 2000; and the Catalina Sky Survey, Larson et al. 1998, and others; see Jedicke et al. 2015 and references therein) have been among the principal asteroidal science data providers in the past 30 yr. These surveys have significantly increased the number of detected and characterized near-Earth asteroids (NEAs), with notable implications for planetary defense. Asteroid detection and characterization (i.e., optical surveys) have provided mission support by identifying spacecraft mission targets and enabled population studies to refine our understanding of past and future

interactions among a variety of different-sized objects in our solar system. However, surveys are not intended to provide a detailed characterization of individual NEAs, which is commonly achieved with subsequent ground-based telescopic follow-up.

The recently spacecraft-visited potentially hazardous asteroids (PHAs) Bennu (DellaGiustina et al. 2021) and Ryugu (Sugimoto et al. 2021) have revealed spectrally distinct bright boulders on their surfaces. Furthermore, these spacecraft observations raise the question of whether it is common for NEAs to possess heterogeneous surfaces. Examples of some asteroids that have shown spectral variability include (4) Vesta (Gaffey 1983; Reddy et al. 2012a) ($D = 525.4$ km; Russell et al. 2012), (16) Psyche (Sanchez et al. 2017) ($D = 226$ km; Shepard et al. 2017), 3200 Phaethon (Lazzarin et al. 2019) ($D = 5.5$ km; Taylor et al. 2019), and the active asteroid (6478) Gault (Marsset et al. 2019) ($D = 2.8$ km; Devogèle et al. 2021). Radar circular polarization ratio (CPR) variation was also observed across the surface of 2006 AM₄ (Virkki et al. 2014) ($D \sim 0.17$ km).

Multiwavelength rotationally resolved ground-based observations are key for detecting, confirming, and characterizing unique surface features (i.e., longitudinal spectral variability on asteroids). Identifying asteroids with particular regolith properties would be crucial to pin down targets for future space missions and planning and to develop accurate mitigation strategies (i.e., planning an orbit deflection to a highly porous rubble pile versus a monolith asteroid would require special considerations of the regolith nature).



Original content from this work may be used under the terms of the [Creative Commons Attribution 4.0 licence](#). Any further distribution of this work must maintain attribution to the author(s) and the title of the work, journal citation and DOI.

Table 1
Radar Observations of JD₁ with the Arecibo Planetary Radar System

Arecibo Start Date and Time (UT)	Observation Types	Duration Δt (minutes)	Power (kW)	Δ (au)	B (Hz)	Visible Range Extent (m)	Runs (CW, Ranging)
1	2	3	4	5	6	7	8
2019-11-01 22:31:55	CW, 1 μ s	90.85	311	0.035	0.9	150	10, 9
2019-11-02 22:53:49	CW, 1 μ s, 0.2 μ s, 0.05 μ s	147.72	299	0.034	1.0	150, 100, 150	20, 94
2019-11-03 23:31:27	CW, 0.05 μ s	24.82	327	0.033	0.9	75	7, 10

Note. Column 1 shows the UT start date and time of the observation, and column 2 shows the types of observations performed. The time (μ s) translates the spatial resolution of the phase-modulated setup (such time does not apply to the CW setup). Column 3 shows the total observational time (Δt , including the time duration of both CW and ranging observations), column 4 shows the average transmitted power in kilowatts, column 5 shows the distance in astronomical units, column 6 shows the observed CW Doppler frequency bandwidth in hertz, column 7 shows the maximum visible range in meters, and column 8 shows the number of completed transmit–receive cycles for CW setup and ranging (the number of ranging cycles corresponds to the total number, in case of multiple phase modulations).

Table 2
Spectroscopy and Photometry Observations of JD₁

Date (UTC)	Time of Observations	Telescope	Phase Angle (deg)	V Magnitude
2019 Nov 1	01:39:32	LDT	68	15.9
2019 Nov 7	10:24:26	LCO	40	15.3
2019 Nov 21	15:04:33	LCO	50	18.1

Here we present results from our parallel multiwavelength and multifacility observational campaign of the NEA 2015 JD₁ (hereafter JD₁). It is an Apollo-like NEA classified as a PHA by having an Earth minimum orbit intersection distance (MOID) of 0.023 au and an absolute magnitude, H , of 20.62 (asteroids with MOID < 0.05 au and H < 22 are classified as PHAs).⁸ Previous observations of JD₁ found a rotation period of 5.2116 ± 0.0006 hr (Warner & Stephens 2020) and an L-type taxonomic classification (Perna et al. 2018) based on visible spectra.

2. Observations and Data Reduction

We performed near-simultaneous observations of JD₁ using the Lowell Discovery Telescope (LDT) and Arecibo Observatory in 2019 November. Observations from Las Cumbres Observatory (LCO) during the 2019 apparition are also presented in this work. This multiwavelength approach allows us to use complementary techniques to constrain a range of physical properties for this object, including its apparent shape, size, scattering properties, composition, taxonomic classification, density, and geometric albedo. Observational circumstances for the Arecibo data are provided in Table 1 and for LDT and LCO in Table 2.

2.1. Arecibo Radar Observations

Radar observations of JD₁ were carried out using the Arecibo Observatory S-band (2380 MHz; 12.6 cm) planetary radar system from 2019 November 1 to November 3, including when JD₁ was at its closest approach of 0.033 1 au from the Earth on November 3. Both Doppler echo power spectra and delay-Doppler imaging were collected during the 3 days.

A typical Arecibo radar observation of an NEA consists of transmitting a monochromatic, circularly polarized signal either unmodulated (continuous wave, CW) or modulated (ranging or images). The transmit–receive cycle consists of transmitting for one light round-trip time to the target, then receiving the echo

for an equal time. The transmitted power was ~ 300 – 400 kW during the observations. For a detailed description of the radar procedure, see Ostro (1993).

The received echo was recorded in the same-circular (SC) and opposite-circular (OC) polarizations. For an ideally smooth mirrorlike surface, the reflected signal is expected to be returned in OC only. The returned depolarized signal indicates the presence of both quasi-specular and diffusive scattering properties from the surface. Hence, the ratio of the SC to the OC polarization, the so-called CPR, was computed to understand the degree of possible surface undulation and composition.

A total of 37 transmit–receive cycles on the CW setup were acquired during the scheduled radar observations (see Figure 1 for visualization of the weighted sum CW spectra per day). Delay-Doppler imaging was performed at 7.5 m range resolution during the 3 days of observations. To obtain the radar images, we converted the echo power into z -score normalized images (see Figure 6). For each observation, we performed CW scan-by-scan verification and selected those with a robust signal-to-noise ratio. Table 1 provides a detailed summary of the radar observations. A detailed description of the radar observations of JD₁ (i.e., systematic issues and observation methods) will be provided in Virkki et al. (2022).

2.2. LDT: Near-infrared Spectroscopy

Near-infrared (NIR) observations of JD₁ were conducted at the 4.3 m LDT in Happy Jack, Arizona, on 2019 November 1, while the asteroid was 0.037 au (14.7 lunar distances) from Earth and with a brightness of $V = 15.9$ (Table 2). We used the Near-Infrared High Throughput Spectrograph (NIHTS) at LDT. The NIHTS is a low-resolution NIR spectrograph that covers the wavelength range from 0.86 to 2.4 μ m in a single order (Dunham et al. 2018; Gustafsson et al. 2021). The LDT instrument cube is equipped with a dichroic fold mirror that transmits the visible wavelengths and reflects the NIR, allowing for simultaneous visible imaging with the Large Monolithic Imager (LMI) and NIR spectroscopy with NIHTS.

⁸ https://cneos.jpl.nasa.gov/about/neo_groups.html

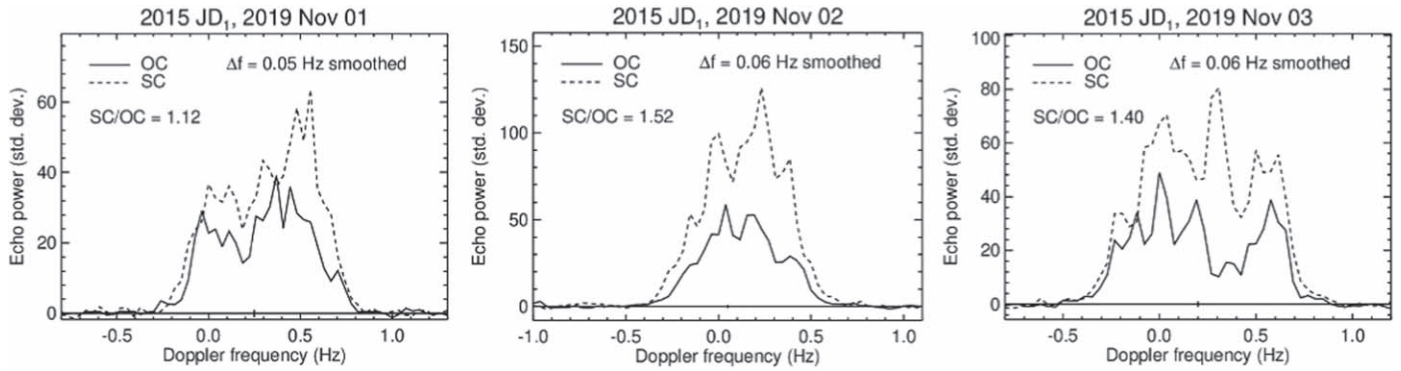


Figure 1. Doppler-only echo power spectra of JD₁ from 2019 November 1–3 using the Arecibo S-band planetary radar system. Echo strength in both the OC (solid line) and SC (dashed line) polarization as transmitted is shown. The echo power on the Y-axis is measured in standard deviations of the background noise. The effective frequency resolution (Δf) is smoothed to 0.05/0.06 Hz. Over the 3 days of observations, diffuse scattering dominates the reflection.

The NIR spectra of JD₁ were obtained with NIHTS in the low-resolution ($R \sim 50$) $4'' \times 12''$ slit, oriented north to south. At the beginning of the observation, we performed dome flats and arc-lamp calibrations. Dome flats were collected with dome lamps of 4700 K and 12 V inside the dome. We used the xenon arc lamp mounted inside the instrument to generate spectral calibration lines (see Gustafsson et al. 2021 for more details on the NIHTS observing procedure). We tracked JD₁ at its sky motion rate near the meridian while the airmass ranged from 1.01 to 1.04 to minimize atmospheric dispersion. The data were acquired by nodding the object with $5''$ offsets along the spatial direction of the slit between the A and B positions in an ABBA pattern. We used a 120 s exposure time to optimize both signal and wavelength coverage. The ABBA nod pattern with 120 s exposures was repeated for 2.8 hr of observation, resulting in a total of 19 spectra shown in Figure 2. The conditions during the observation remained relatively clear, with some wind and thin clouds (seeing ranged from $1''.4$ to $1''.7$). The precipitable water value was approximately 1.1–1.8 mm.⁹ To correct for telluric absorption and obtain relative reflectance, the solar analog star SA 113-276 was observed at similar airmass to the asteroid. The standard data reduction procedures were performed using the IDL *Spextool* package (Cushing et al. 2004), which has been adapted for NIHTS. Figure 2 shows the whole spectral data set covering $\sim 56\%$ of the JD₁ period (5.2116 ± 0.0006 hr; Warner & Stephens 2020).

2.3. LDT: Photometry

We obtained simultaneous visible photometry of JD₁ with LMI through the dichroic fold mirror (Massey et al. 2013). Observations were conducted in Sloan Digital Sky Survey (SDSS) *g*- and *r*-band filters. The full LMI field of view captures $12'.5 \times 12'.5$ with a 6144×6160 pixel CCD camera with an unbinned pixel scale of $0''.12$ pixel⁻¹. The transmitted optical beam through the dichroic fold mirror creates a roughly oval-shaped unvignetted field of view of $6'.5 \times 4'.0$. Within this field, the throughput loss on the *g* and *r* filters is $\sim 10\%$ (Gustafsson et al. 2021). Images were obtained in 2×2 binning mode ($0''.24$ pixel⁻¹) with exposure times ranging between 4 and 5 s. Flat-field images were taken for the *g* and *r* filters during astronomical twilight on 2019 November 1. All data were bias-subtracted and flat field-corrected for their corresponding filters.

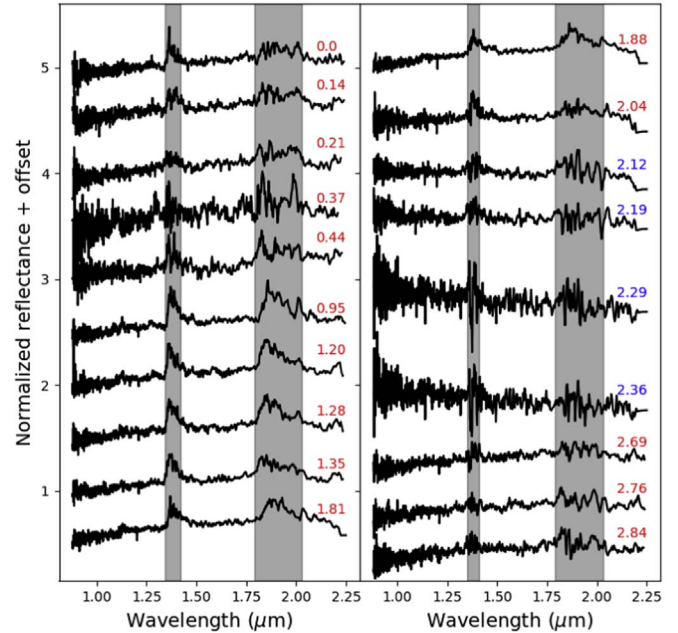


Figure 2. Rotational NIR spectra of JD₁ obtained from LDT at Happy Jack, Arizona. The spectra have been organized from the beginning (first spectrum obtained at 01:39:32 UT on 2019 November 1) to the end of the observation from top to bottom and left to right. Each spectrum has been normalized to unity at $1 \mu\text{m}$ plus an offset added in the reflectance for clarity. Gray shaded areas indicate wavelengths of telluric absorption. The numbers at the end of each spectrum (around $2.2 \mu\text{m}$) indicate the time in hours at which the spectrum was obtained after the first scan. Red numbers refer to those spectra that appear red (positive slope), while blue ones refer to those that look blue (negative slope). The raw and calibration data for these rotational NIR spectra are available as data behind the figure.

(The data used to create this figure are available.)

The reduced LMI imaging data were analyzed using the automated Photometry Pipeline (PP; Mommert 2017). The PP first utilizes SExtractor (Bertin & Arnouts 1996) to identify objects within each field, then SCAMP (Bertin 2006) is called to match all sources with the selected photometry catalog. The astrometry was performed using data from the Gaia (DR1) mission (Gaia Collaboration et al. 2016). The Pan-STARRS (Chambers et al. 2016) and SDSS (Ahn et al. 2012) catalogs were individually used to perform the photometry. Astrometry and photometry catalog queries were executed via PP using the VizieR Catalog Service (Ochsenbein et al. 2000). We performed

⁹ <http://weather.uwyo.edu/upperair/sounding.html>

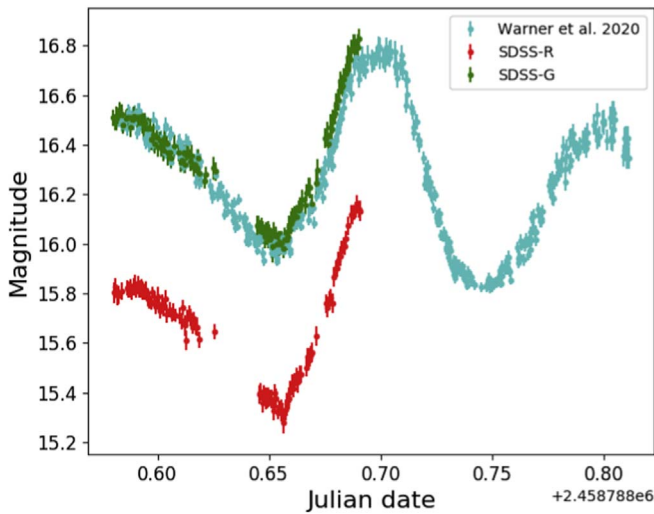


Figure 3. The SDSS *g*- (green dots) and *r*-band (red dots) filter light curves of JD_1 as a function of time since the beginning of the observation obtained using the LMI at LDT. These single-peaked light curves show half of JD_1 's bimodal light curve, shown in cyan dots, from Warner & Stephens (2020). The gap in the LDT data between 1.3 and 1.7 hr corresponds to the observation of the standard star. The *g* and *r* light curves are available as data behind the figure, and the raw photometry data are made available on FigShare: <https://doi.org/10.6084/m9.figshare.20137265.v1>.

(The data used to create this figure are available.)

manual and visual identification of the target for the whole set of images to discard images where the target was passing over or near a star or cosmic ray and to ensure correct target identification during the automated process. We manually verified a random sampling of results using the Aperture Photometry Tool (Laher et al. 2012). We performed another PP calibration using only stars with solar-like colors to compare with the automated photometric analysis and obtain a more reliable photometric reduction. Ultimately, 115 and 105 data points were obtained for the *g*- and *r*-band filters, respectively. We interpolated the light curves in Figure 3 using the *interp* routine of the *numpy* Python package to obtain the respective *g* and *r* magnitudes at equal times.

2.4. LCO: Visible Spectroscopy

In this paper, we also present visible spectroscopic observations obtained by LCO using the FLOYDS¹⁰ spectrographs located on the 2.0 m telescopes in Haleakala, Hawaii, and Siding Springs, Australia, on 2019 November 7 and November 21 at UTC 10:24:26.7 and 15:04:33.1, respectively. The data shown in Figure 4 are the smoothed, reduced spectra that were scheduled, observed, and reduced via a fully remote and automated process using the NEOExchange observation portal (Lister et al. 2021) and the LCO automated pipeline.¹¹ Exposure times of 1800 and 3600 s were used, while airmass ranged from 1.4 to 1.6 and 1.1 to 1.3 for the November 7 and November 21 observations. The solar analogs HD 60298 and SA 93 were observed near the target for the November 7 and November 21 observations. On November 21, the JD_1 *V* mag was ~ 18.1 , resulting in a poorer-quality observation.

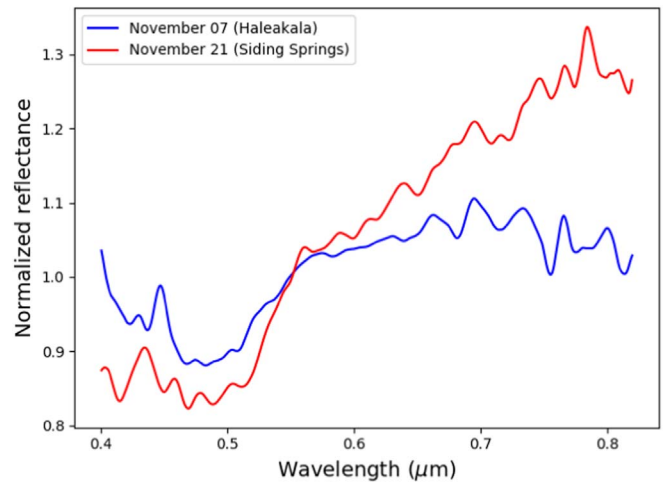


Figure 4. Visible spectra obtained at Haleakala Observatory, Kula, Hawaii, and Siding Springs, Australia, from LCO. Blue and red lines are the visible spectra obtained on 2019 November 7 and November 21, respectively. Both spectra have been normalized to unity at $0.55 \mu\text{m}$. The raw and calibration data for these visible spectra are available as data behind the figure.

(The data used to create this figure are available.)

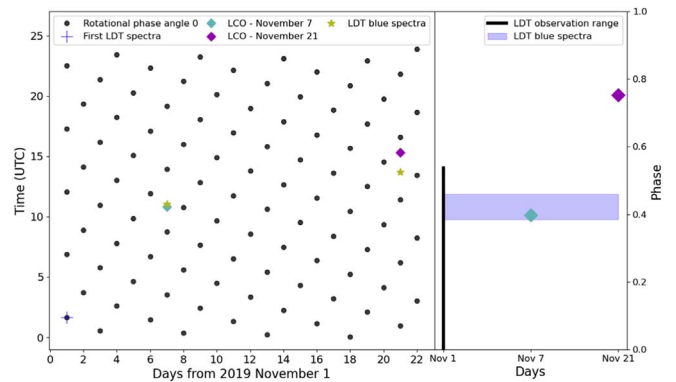


Figure 5. Left: track of JD_1 's rotational phase angle 0° , defined as the orientation of the first LDT spectra obtained at 01:39:32.37 UTC on November 1, as a function of days (gray filled circles). The yellow star indicates the time of observing the blue spectra at LDT. The cyan and magenta diamonds illustrate the LCO observations. Right: phase range of each observation per day of the observation. The blue shaded area illustrates the phase range of the blue NIR spectra at LDT. The black line shows the range of the LDT observation, while the diamonds represent each LCO observation in the corresponding phase. The measurement uncertainties are shown in the text.

We phased the LCO observations to our LDT observation to check if we were likely observing the same object geometry. In Figure 5, we present the tracking of the zero (0°) rotational phase angle (Θ_0 , beginning at UTC 01:39:32.37 on November 1) or the orientation that we were observing on the first scan obtained at LDT-NIHITS by adding JD_1 's rotation period (5.2116 ± 0.0006 hr; Warner & Stephens 2020). Because LCO observations were performed several days after our LDT observation, we also considered the relative offset induced by sky motion when phasing these observations. On November 7 and November 21, we find that the LCO observations were 28° and 18° , respectively, different in phase angle from where we were looking with LDT on November 1 (68°). The difference in phase angles imposes an offset of +25 and +15 minutes to the derived Θ_0 for November 7 and November 21, assuming a prograde rotation. We find that the LCO spectrum from

¹⁰ <https://lco.global/observatory/instruments/floyds/>

¹¹ <https://lco.global/documentation/data/floyds-pipeline/>

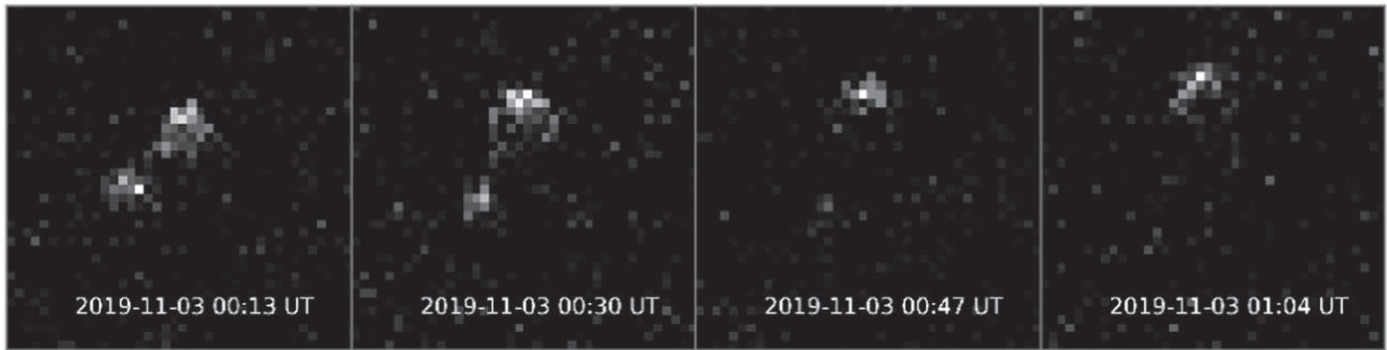


Figure 6. Compilation of Arecibo delay-Doppler images of JD₁ from 2019 November 3 showing roughly one-sixth of its full rotation. In each frame, the resolution is 7.5 m pixel^{-1} (vertical) \times $0.0745 \text{ Hz pixel}^{-1}$ (horizontal). Each radar image is the weighted sum of 15 consecutive transmit/receive cycles. Time increases from left to right and is indicated at the bottom of each panel.

November 7 (cyan diamonds in Figure 5) corresponds to the orientation we were observing for JD₁ at the LDT around $2.36 \pm 0.02 \text{ hr}$ after Θ_0 (yellow star in the left panel or blue shaded area in the right panel). The observation from November 21 (magenta diamonds) covered an orientation not observed by the LDT observations, specifically, $4.86 \pm 0.06 \text{ hr}$ after Θ_0 , or 2.02 hr after the last spectrum presented in Figure 2. In summary, the bluer LCO visible spectrum from November 7 coincides with the orientation we were observing for the blue sloped NIR spectra at LDT on November 1, while the steeper red LCO spectrum corresponds to an orientation that we did not cover at LDT (see the right panel of Figure 5 for better data visualization). Furthermore, both LCO and LDT observations support spectral variability in a similar near-surface region on JD₁.

3. Results

3.1. Constraining Composition and Physical Properties

Arecibo delay-Doppler images reveal a contact binary asteroid with an elongated projection, as expected from the 0.9 mag light-curve amplitude (Warner & Stephens 2020). The bilobed structure presented in Figure 6 shows a body and head of approximately 100 and 50 m, respectively, or around 150 m in visible extent (see Figure 7). Radar images and CW experiments show no evidence of separate binary structure, which usually appears as a delta peak in the Doppler-only echo power spectra (Naidu et al. 2020).

The disk-integrated CPR, the quotient of the diffuse and quasi-specular integrated echo power (SC/OC), is 1.35 ± 0.54 on average and 1.12 ± 0.29 , 1.52 ± 0.40 , and 1.4 ± 0.22 on November 1, November 2, and November 3, respectively (see Figure 1 for data visualization). Object JD₁ has one of the highest and most consistent disk-integrated CPR values ever reported among other radar NEAs (Benner et al. 2008; Aponte-Hernandez et al. 2020). We should point out that the system temperature of the Arecibo S-band radar system suffered some issues due to the low-noise amplifier (LNA) degradation after 2019 April. The LNA issue could have produced lower measurements of OC cross sections, thus yielding additional uncertainty on the CPR values. We attempted to address this issue in the data reduction. It seems statistically unlikely that JD₁'s high CPR measurements were affected by this issue because of the consistency over the 3 days of radar observations. More discussion about the LNA issue and how

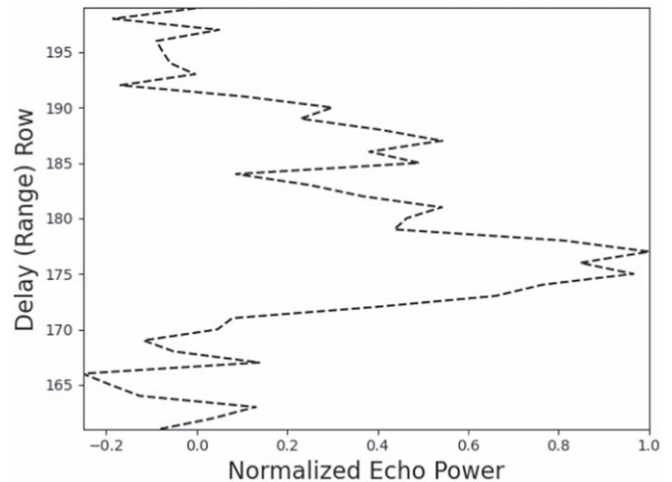


Figure 7. Distribution of echo power as a function of normalized echo depth, made by collapsing the horizontal dimension of the range-Doppler image. The strong signal in at least 20 rows at 7.5 m pixel^{-1} suggests $\sim 150 \text{ m}$ along the long axis.

it may have affected Arecibo's S-band radar observations can be found in Virkki et al. (2022).

The measured total radar cross section, σ_T , given by the sum of the geometric OC and SC cross sections, of JD₁ on November 2 and November 3 is 6356 ± 146 and $11911 \pm 158 \text{ m}^2$, respectively, with a systematic calibration uncertainty of 25%. In other words, for example, if JD₁ were a perfectly isotropically reflecting metal sphere of 6356 m^2 geometric cross section, it would return the same amount of power if observed under similar circumstances. Assuming JD₁ is a sphere of 0.15 km, its upper limit OC ($\hat{\sigma}_{OC}$) and SC ($\hat{\sigma}_{SC}$) radar albedo (the ratio of the radar cross section of a given polarization by the derived effective projected area) would be 0.22 ± 0.05 and 0.31 ± 0.08 , respectively, or a total radar albedo $\hat{\sigma}_T = 0.53 \pm 0.10$. Additional uncertainty in the radar albedo could arise from deviation in the projected area (i.e., highly elongated asteroids), which can add an offset of 25% to the radar albedo computed above.

3.2. Subradar Point

The spin axis of a celestial body can be constrained from radar by measuring the change in the subradar latitude point. As the asteroid rotates, one limb approaches the line of sight while the other rotates away such that the transmitted

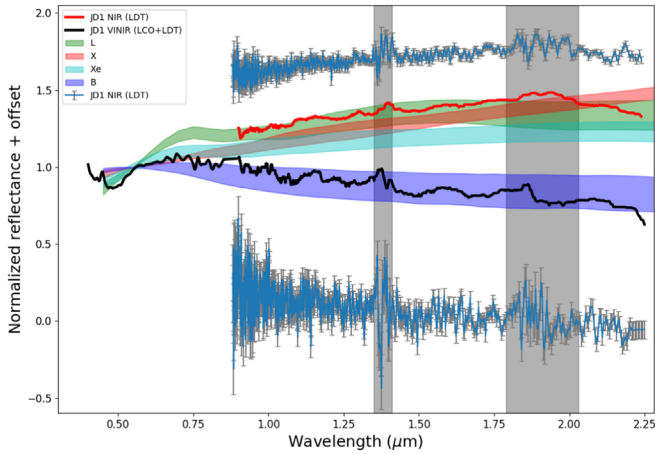


Figure 8. Visible and NIR spectra of JD_1 obtained at LCO and LDT. The top and bottom blue solid lines correspond to the featureless nonsmoothed spectra of JD_1 obtained at LDT. The red, cyan, green, and blue shaded areas are the $\pm 1\sigma$ spectra of X-, Xe-, L-, and B-type asteroids, respectively, from Bus–DeMeo taxonomy. Bus–DeMeo and JD_1 visible and NIR spectra have been normalized at $0.55 \mu\text{m}$. The gray shaded areas indicate residual telluric features from the data reduction. Both NIR spectra from LDT (blue spectra) have been normalized to unity at $1 \mu\text{m}$ plus an offset in reflectance for clarity.

monochromatic signal is broadened in Doppler. For a spherical with rotation rate P , the broadened received signal in an echo bandwidth B is given by

$$B(\phi) = \frac{4\pi D(\phi)}{\lambda P} \cos(\delta), \quad (1)$$

where $D(\phi)$ is the breadth of the asteroid at rotation phase ϕ , λ is the wavelength of the transmitted signal (0.126 m), and δ is the subradar latitude on the asteroid as viewed by the observer. Although JD_1 is not a spherical object, this expression holds for any irregular (nonspherical) object. We modeled JD_1 's Doppler dispersion bandwidth (shown in Figure 1) using Equation (1).

In Equation (1), the subradar latitude variability is limited by the change of Doppler dispersion when the rotation period and sphere diameter are well established. Figure 1 shows small Doppler dispersion differences at each observation, which will induce negligible subradar latitude changes. We found that an effective diameter of 150 m with a rotation period of 5.2116 hr yields a Doppler dispersion of $\sim 0.9 \text{ Hz}$ if JD_1 was observed at or near its equator (around $\pm 70^\circ$ from the pole). The largest observed bandwidth of $\sim 1.2 \text{ Hz}$ on November 3 requires an effective diameter of around 190 m , also suggesting a near-equator subradar latitude point. Furthermore, our solutions support the rotation period derived by Warner & Stephens (2020). In addition, Figure 6 shows the smaller lobe disappearing as the body rotates, which is evidence of a subradar latitude near the equator (i.e., if the subradar point were far off the equator, both lobes would be visible the whole time).

3.3. Spectroscopic Variation and Photometric Color

In Figure 8, we present two of 19 featureless NIR spectra of JD_1 : a positive-slope (top) and a negative-slope (bottom) spectrum. These spectra were selected to illustrate the differences between their slopes. The negative-sloped (blue) and positive-sloped (red) NIR spectra correspond to the spectra obtained at 2.29 and 2.69 hr at LDT with NIHTS shown in Figure 2. With black solid lines, we show the visible and NIR

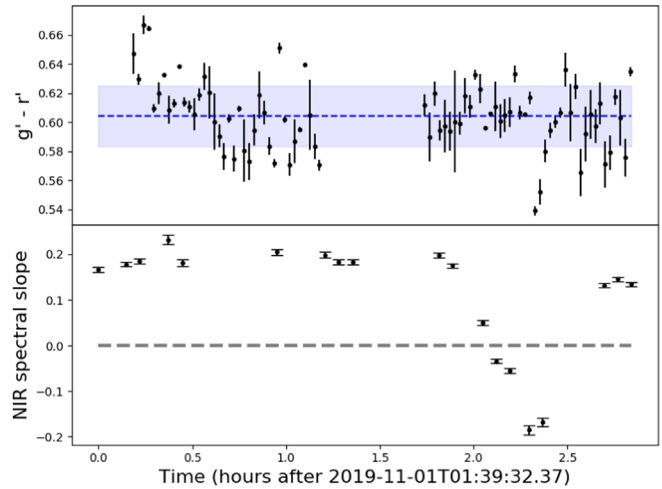


Figure 9. Top panel: Sloan $g' - r'$ color variation as a function of time since the beginning of the LDT observation. The horizontal dashed blue line and blue shaded area indicate the average $g' - r'$ color and standard deviation, respectively. Bottom panel: NIR continuum–spectral slope variation as a function of time since the beginning of the observation. Slope variation can be noticed after $\sim 1.9 \text{ hr}$.

spectra of JD_1 . The NIR spectra were smoothed using a median filter from the *Scipy* Python package and offset to match the normalized visible reflectance from LCO. The nonsmoothed red and blue NIR spectra (blue line) are plotted above and below to their respective smoothed spectra. The most likely Bus–DeMeo spectral classifications are plotted in Figure 8 as red, cyan, green, and blue shaded areas for X-, Xe-, L-, and B-types, respectively, and suggest spectroscopic similarities between these taxonomies: X-complex and B-type classification for the red and blue spectra of JD_1 , respectively.

Perna et al. (2018) classified JD_1 as an L-type asteroid. The L-type spectra are characterized by the positively sloped visible spectra with a gentle concave curvature around $1.5 \mu\text{m}$. The red visible and NIR spectra of JD_1 appear like an L-type but also are not too different from an Xe-type. Distinguishing between these two taxonomies is often very complicated because of the spectral similarities. The NIR spectra of JD_1 lack concave and convex curvatures around 1.5 and $2.0 \mu\text{m}$, respectively (see Figure 2), which are characteristic features of L-types (Devogèle et al. 2018). Additionally, the absorption band feature of JD_1 around $0.5 \mu\text{m}$ (see Figure 4) is typical of sulfide minerals such as oldhamite, seen on E-types (Clark et al. 2004). This spectral analysis combined with our radar measurements suggests that JD_1 is likely an X-complex/E-type. Although our observations suggest an E-type taxonomy, the red spectra of JD_1 closely resemble L-types. It is critical to mention that L-types are extremely rare primitive asteroids that constitute a very small fraction of objects in the main belt of asteroids (Devogèle et al. 2018).

Laboratory and telescopic studies have proved NIR spectral variability due to differences in phase angles, atmospheric dispersion, grain sizes, surface refreshing, observational circumstances (i.e., instrumental failure, target out of slit, or stellar interference), space weathering, and/or mineralogical composition.

The NIR spectral slope variability observed in JD_1 (bottom panel, Figure 9) is transitional: a consistent positive slope observed for about 2 hr after the first measurement, changing to a blue negative slope for $\sim 0.5 \text{ hr}$ and eventually transitioning

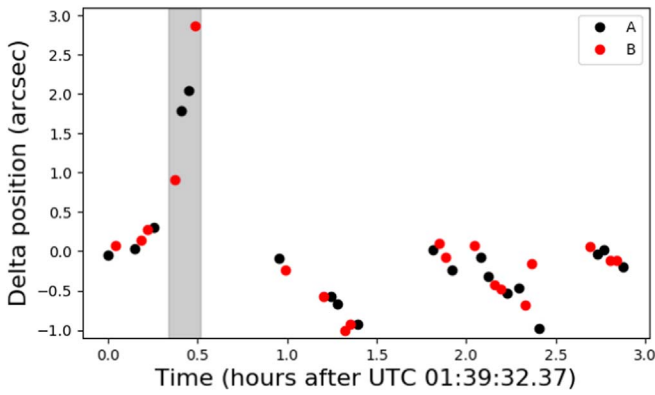


Figure 10. Pixel shift of JD₁ as a function of time (starting at 01:39:32 UTC). Black and red circles are the delta central aperture position of each spectrum at the A and B slit positions, respectively. The gray shaded area indicates the timing of the largest slit drift (spectral variability occurs after ~ 1.9 hr).

back to red positive-sloped spectra. The variability suggests that any of the previous factors could be affecting our spectroscopic result. However, we can conservatively discard some of them.

Spectroscopic studies (i.e., Nathues 2010; Reddy et al. 2012b; Sanchez et al. 2012) have shown the increase/decrease of the spectral slope and band depth when the phase angle g increases in the range $0^\circ < g < 120^\circ$. The phase angle of JD₁ decreased from 68° to 67° from the beginning to the end of the observation at the LDT. The change in phase angle is about 0.5° , too small to be responsible for the observed spectral variability. Thus, we can confidently discard the phase angle factor.

The observed spectral variability (bottom panel, Figure 9), does not suggest a phase angle-like variability but offers the possibility of an observational failure, i.e., the asteroid moving out of the slit. If the slit was not consistently aligned in the same way for every exposure in either position A or B, then, in theory, there could be a shift in intensity that is wavelength-dependent. If the slit was fixed, as during our observation, any fraction of light lost due to a finite slit would be the same for every exposure at each wavelength. We used *Spextool* to measure the central aperture slit position as a function of time. Figure 10 shows JD₁'s aperture shift in the $4''$ slit as a function of time. The timing of the largest drift does not line up with the change in NIR spectral slope we found in JD₁. At the time of observing spectral variability, we found a drift of $< 1''$ (~ 9 pixels) between the asteroid and the slit. Thus, the possibility that the asteroid was moving out of the $4''$ slit during the time of the spectral slope change can be rejected.

Another factor that we considered is the atmospheric dispersion. However, this could be easily discarded, given that JD₁ was observed at relatively low airmasses between 1.01 and 1.04. We verified the standard star slopes and found similar normalized spectral slopes with no difference larger than 2% in continuum. We found consistency in our data reduction (i.e., no correlation between standard star slopes and JD₁'s variability). We performed an inspection of our spectral data and found no stellar interference contaminating JD₁'s flux within the $4''$ slit in our data set.

With the provided overview, it does not seem feasible that our data were affected by observational artifacts. We explore other possibilities that could be causing such spectral variabilities in the next sections. However, such possibilities

support the position that the observed variability truly reflects the surface properties of JD₁.

The average $g' - r'$ color of JD₁ is 0.60 ± 0.03 , shown in the top panel of Figure 9 with a blue dashed line. This color, within the errors, falls in the range of $g' - r'$ colors (0.4–0.6) for X-types (Ivezić et al. 2001). It is well known that asteroid colors reflect the properties of their composition. We also look for visible color variation in order to validate any spectral variation seen in the NIR. The color variation, shown with black dots in the top panel of Figure 9, supports color blueing from 0 to 0.7 hr and around 2.35 hr. While there is a visible color change in JD₁ around 2.35 hr, it is statistically of low significance to support the NIR spectral slope variability, also considering the noisy rotational color distribution. The largest visible color drop occurs around the bluer NIR spectra, while no color decrease is observed at 1.9 hr when the NIR slope changes. This could be due to a nonsimultaneous spectroscopic variability between the visible and NIR region or the noise in the photometric color distribution.

While the completeness and reliability of JD₁ NIR spectral variation are supported by a single observation night of $< 60\%$ of JD₁'s period and thus not confirmed, independent observations from LCO also suggest visible spectral variability. We demonstrated in Section 2.4 that the geometry observed with the blue NIR spectra from LDT coincides with that of the blue visible LCO spectrum. Therefore, we interpret the NIR slope variability as a true reflection of particular surface properties of JD₁ and not as artifacts in the observations. Still, further observational validation is needed.

4. Analysis

4.1. Visible Albedo

We investigated the propagation of visible albedo solutions considering two different diameters and three absolute magnitudes (H) for each diameter (see below for the details of the adopted methodology).

It is known that H mag is the main driver to derive the albedo uncertainty because of the difficulty in measuring the entire asteroid's phase curve (Masiero et al. 2021). We used the $H-G$ (Bowell et al. 1989) system to calculate the absolute magnitude H_f at a given photometric filter f . We used our measured visible magnitudes at the SDSS g - and r -band filters, $V_g = 16.25$ and $V_r = 15.65$; a G -slope value of 0.15; and phase angle $\alpha = 68^\circ$. We obtained the g - and r -band absolute magnitudes $H_g = 21.03$ and $H_r = 20.36$, respectively. In our visible albedo analysis, we also considered the Minor Planet Center absolute magnitude $H_{\text{MPC}} = 20.62$. We used the Fowler & Chillemi (1992) empirical expression that relates the absolute magnitude H , diameter, and visible albedo of an asteroid. By using a fixed diameter of 150 m, we obtained a visible albedo ranging from 0.30 to 0.56 and 0.19 to 0.35 assuming a 190 m effective diameter (see Table 3 for detailed solutions). The range of possible visible albedo solutions gives an average albedo p_{ave} of 0.35 ± 0.12 . The average visible albedo, within the standard deviation, falls in the range of albedos for enstatite-like asteroids (~ 0.4 to ~ 0.6 ; Zellner et al. 1977, 1985; Clark et al. 2004; Thomas et al. 2011) and with the $0.50^{+0.30}_{-0.24}$ derived by Trilling et al. (2016) for JD₁.

Table 3
Visible Albedo (p) Solutions of JD_1 for a Range of Effective Diameters and Absolute Magnitudes

	Absolute Magnitudes		
	H_g 21.03	H_{MPC} 20.62	H_r 20.36
Visible Albedo			
p ($D = 150$ m)	0.30	0.44	0.56
p ($D = 190$ m)	0.19	0.28	0.35
p (average)	0.35 \pm 0.12		

4.2. Meteorite and Asteroid Connections

We have presented evidence that supports a relationship between JD_1 and E-types asteroids, such as the high albedo of JD_1 , high CPR, spectral shape similarities, and near-surface bulk density. We performed a search through the Reflectance Experiment Laboratory (RELAB)¹² database to constrain the composition and trace the possible meteorite connection with JD_1 . We searched for enstatite achondrite meteorites (aubrites) and the common minerals usually present on these meteorites, in which the NIR spectral properties were mostly featureless (Cloutis et al. 1990).

Aubrites are well-known brecciated meteorites chemically dominated by low-iron enstatite (75–98 vol%) with a relatively small amount of plagioclase (4.3 vol% on average) and nearly FeO-free diopside (2.2 vol% on average) and forsterite (3.5 vol% on average; Waters & Prinz 1979; Gaffey 1983; Keil 2010). Bulk chemical analysis indicates that oxides such as MgO and SiO₂ are the most abundant, while CaO, Na₂O, and Al₂O₃ are less abundant. Other metallic elements (Fe and Ni) and sulfides (Ti, Mn, and Cr) are also found to be less abundant. The chemical composition overview of aubrites gives an idea of what elements should be expected on E-types. In Figure 11 (left panel), we show the reflectance of well-known aubrites and the common minerals on them. By visible inspection, spectral slope similarities can be noticed between the JD_1 red and blue spectra and aubrites such as Peña Blanca and ALH 78113.

We have implemented the E-type subclassification techniques developed by Clark et al. (2004) and Gaffey & Kelley (2004) to investigate the composition of JD_1 . Gaffey & Kelley (2004) proposed three subclasses for E-types: E[I], E[II], and E[III]. The E[I] show a slightly curved spectrum with no clear mineral absorption features. The E[II] are distinguished by the strong absorption features near 0.5 μm and a weaker one near 0.9 μm . These absorptions are characteristic of oldhamite. The E[III] are characterized by having an almost-flat spectrum that turns to a red slope with a unique absorption feature near 0.9 μm , attributed to enstatite pyroxene with some Fe²⁺. In addition, Fornasier et al. (2008) found that E[II] asteroids had the highest spectral slopes, while E[III] asteroids had flat or negative visible spectral slopes. The Clark et al. (2004) subclassification technique is based on mineralogical compositional similarities to the E-type asteroids (44) Nysa, (64) Angelina, and (434) Hungaria. The Nysa-like are those whose compositional analysis suggests silicate mineralogy with a higher iron content than enstatite and absorption features at 0.9 and 1.8 μm . The Angelina-like are characterized by having absorption features at 0.5 and 0.9 μm , attributed to silicate

mineralogy plus the presence of sulfide and olivine. The Hungaria-like are asteroids whose compositional analysis revealed some olivine and a typical reflectance feature near 0.9 μm .

The Gaffey & Kelley (2004) classification suggests that JD_1 , having a possible absorption feature centered at 0.507 μm and lacking the 0.9 μm feature, is consistent with an E[II] classification. In Figure 11 (right panel), the JD_1 red spectrum is plotted with the E-types (434) Hungaria, (64) Angelina, and (44) Nysa for comparison. Object JD_1 has a red spectrum among the E-types with a particular spectral similarity to (64) Angelina. Using both Clark et al. (2004) and Gaffey & Kelley (2004) classifications, we suggest that JD_1 corresponds to the Angelina-like group, given their spectral similarities observed in Figure 11. The presented spectral connection implies that JD_1 mineralogy should be similar to that of aubrite meteorites plus oldhamite and troilite (Clark et al. 2004).

4.3. Grain Sizes

Spacecraft-visited asteroids (i.e., Itokawa, Bennu, Eros, and Ryugu) have shown that the surfaces of small bodies are highly diverse, with particles ranging from dust- to boulder-like sizes. Such particle variability could affect the deduced spectral composition by making spectra appear distinct at different phase orientations. Meteorite reflectance as a function of composition and grain size would provide crucial information on whether a spectral variation is due to different grain sizes or mineralogical compositions or a combination of both.

If the JD_1 variation is only due to a change in grain size under a similar composition, we should be able to validate this by looking at the reflectance variation as a function of wavelength and grain size. Figure 9 (bottom panel) shows that much of the JD_1 surface is spectrally red. We then considered whether different grain sizes on NIR spectral red meteorites could lead to negative blue spectra. The effect of grain size on iron sulfide (Mundrabilla) and enstatite achondrite (ALH 78113) spectra is illustrated in Figure 12. The reflectance of the aubrite ALH 78113 shows a flat NIR spectral slope for small grain sizes (<45 μm) and a drastic decline in the NIR slope as the grain sizes increase up to chip-sized grains. Similar behavior can be observed for the reflectance of the Mundrabilla meteorite as a function of wavelength. The NIR slopes of ALH 78113 range from -6% to $0.6\% \mu\text{m}^{-1}$, while the NIR slopes of the Mundrabilla meteorite range from 26% to $33\% \mu\text{m}^{-1}$. In other words, the grain sizes of ALH 78113 and Mundrabilla contributed a slope difference (redder slope minus bluest slope) of 6.6% and $7\% \mu\text{m}^{-1}$, respectively. Object JD_1 has an NIR slope difference of $41.71\% \pm 0.01\% \mu\text{m}^{-1}$ (most positive to most negative spectral slope difference). It is clear that grain sizes do have a strong influence on the NIR slope and visible color. However, we have demonstrated that we are unlikely to explain the NIR slope variation of JD_1 with the size range of grains in RELAB. More laboratory work needs to be done on aubrite meteorites or simulant material at a larger range of grain sizes to test the feasibility of the grain size hypothesis. Thus, the scenario where JD_1 's spectral variation could be due to a compositional and grain size heterogeneity seems feasible.

4.4. Color and Albedo: Hints for Mineralogical Composition

The colors of asteroids reflect information about their mineralogical composition, since they can contain diagnostic

¹² <https://sites.brown.edu/relab/>

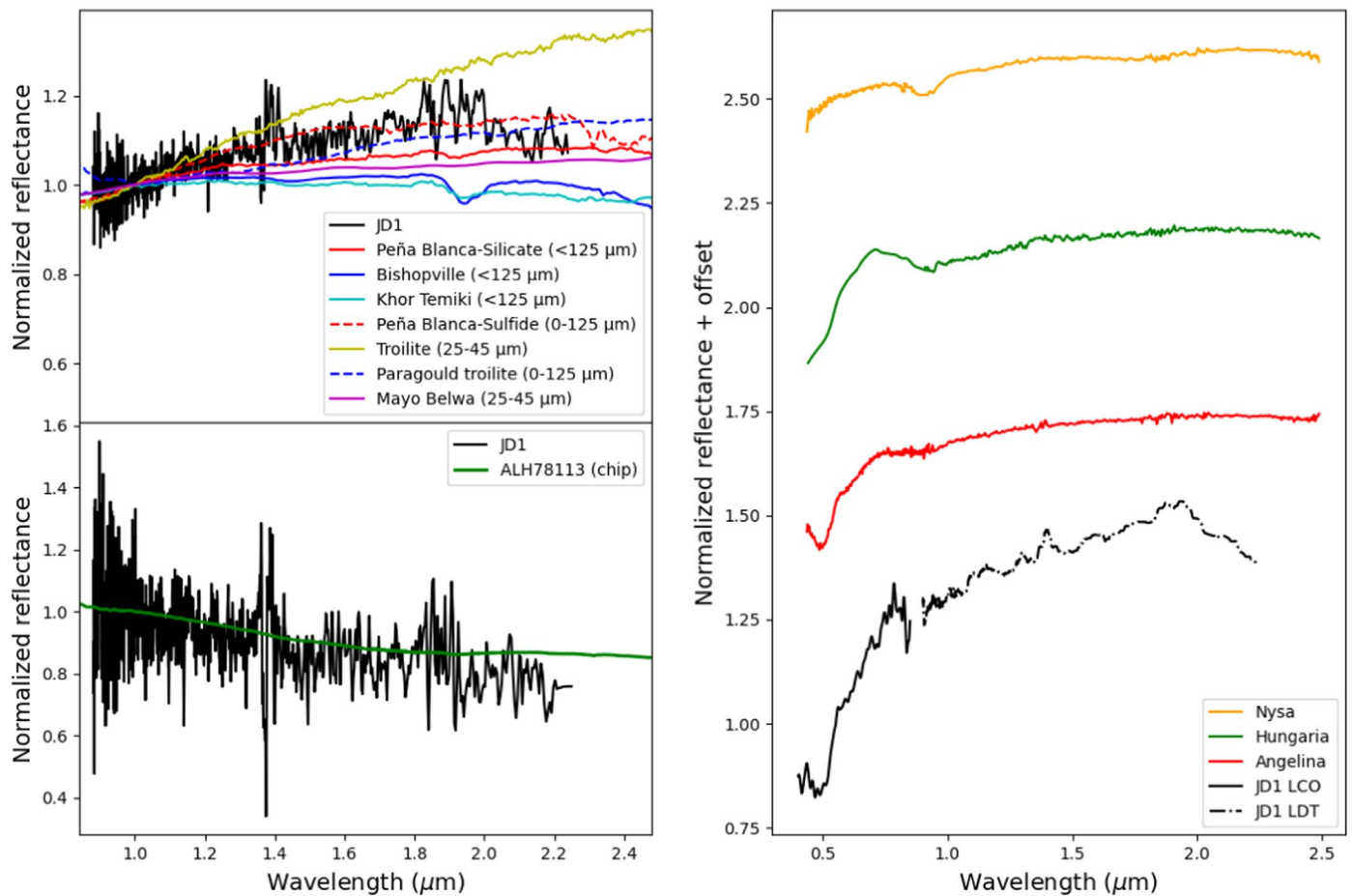


Figure 11. Plot of NIR spectra of JD₁ (solid black line) and selected RELAB meteorites, minerals, and E-type asteroids. Top left panel: reflectance of aubrites Mayo Belwa (RELAB sample code s1tb46), Khor Temiki (RELAB sample code c1tb48), Bishopville (RELAB sample code c1tb47), Peña Blanca silicate and sulfide regions (RELAB sample codes c1tb45 and c1tb55, respectively), and minerals troilite and Paragould troilite (RELAB sample codes cdmb06 and latb50, respectively). Bottom left panel: NIR blue reflectance of JD₁ and aubrite ALH 78113 (RELAB code bkr1ar001). Right panel: JD₁ visible and NIR spectra and E-type asteroids (434) Hungaria, (44) Nysa, and (64) Angelina obtained from Binzel et al. (2001), Clark et al. (2004), and Bus & Binzel (2002), respectively, plus an offset in the reflectance for clarity. The NIR reflectance of JD₁ was smoothed using a median filter from the *Scipy* Python package and offset to match the visible reflectance. All of the spectra in the left and right panels were normalized at 1 and 0.55 μm , respectively.

features of the spectral bands. We developed an analysis to compare JD₁'s visible colors and NIR slopes with meteorites and asteroids presented in Section 4.2. This will help to explore the possible mineralogical composition of the spectral variability. Similarly, we provide an NIR spectral slope and albedo study to investigate possible compositional connections.

To obtain the Sloan $g' - r'$ color, we retrieved the visible spectra of ALH 78113, Mundrabilla troilite, Paragould troilite, troilite mineral, Peña Blanca silicate and sulfide samples, and Khor Temiki from RELAB. We convolved each spectrum with the bandpasses for the Sloan g' and r' filters (Gunn et al. 1998; Doi et al. 2010). From the ratio of these integrated reflectances, we derived the intrinsic visible reflectance color, in magnitudes, for each meteorite. Finally, we add in the $g' - r'$ solar color of Willmer (2018) to produce the apparent color that each meteorite would have if observed in space (that is, as illuminated by the Sun). The LCO intrinsic visible reflectance color of JD₁ was also determined using the same methodology. The LDT-LMI $g' - r'$ colors were selected based on the measured color at the corresponding time of the respective NIR spectra presented in Figure 8. To obtain the $g' - r'$ color of the M- and E-types, we used their $B - V$ colors given by Tedesco (2005) and the color

transformations between the Johnson–Cousins and Sloan systems (Castro et al. 2018).

Figure 13 (top panel) illustrates the NIR spectral slope as a function of the $g' - r'$ color of the selected RELAB meteorites, minerals, M- and E-types, and JD₁ colors. The NIR spectral slope was measured from the 0.8 to 2.5 μm regions. The solid circles in Figure 13 correspond to the observed colors of JD₁ from LDT and LCO. The black and blue circles represent the redder and bluer photometric color from LDT. We adopted the same NIR spectral slopes from the LDT spectroscopic observations as the retrieved colors from LCO visible spectra given that there are no NIR spectra from LCO. However, such an assumption will not affect the purpose of this analysis because when comparing LCO and LDT, we only refer to the visible colors. The retrieved LCO visible colors of JD₁ (magenta and cyan circles in Figure 13) support a color variation similar to that obtained from the photometric observation at LDT. The bottom panel illustrates the NIR spectral slope as a function of albedo. The black boxes (aubrites, nickel-iron, and enstatite chondrites) indicate possible meteorite analog ranges from Gaffey (1976), and the dashed black boxes are the ranges derived from observation of M- and E-types from Bell et al. (1988). The M- and E-type

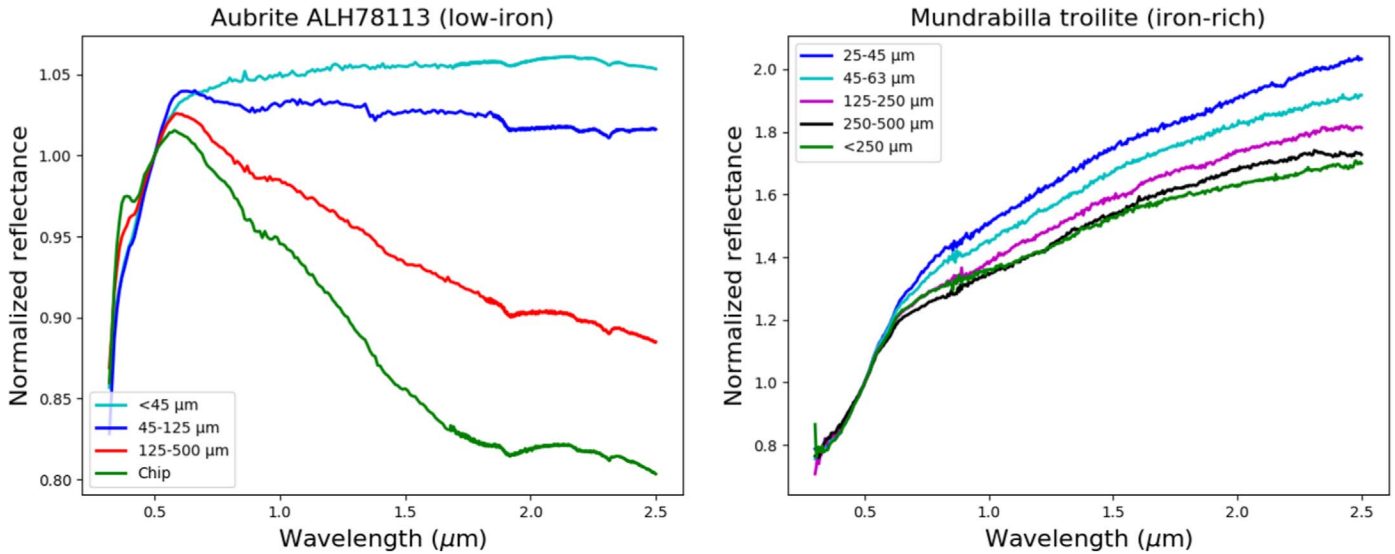


Figure 12. Plot of RELAB meteorite reflectances showing the effect of grain sizes in the NIR slope. Left: reflectance of the aubrite ALH 78113 at different grain sizes (low-iron sample). The RELAB sample codes are bkr1ar001, bkr1ar001a, bkr1ar001b, and bkr1ar001c for ALH 78113 reflectances with grain sizes in the range of “chip” and 125–500, 45–125, and <45 μm , respectively. Right: reflectance spectra of the Mundrabilla meteorite at different grain sizes (iron-rich sample). The RELAB sample codes are cbmb06, ccm06, cemb06, cfmb06, and c1mb06 for Mundrabilla’s reflectances with grain sizes in the range of 25–45, 45–63, 125–250, 250–500, and <250 μm , respectively. Both meteorites’ spectra become bluer as grain sizes increase.

asteroid albedos were obtained from Masiero et al. (2014), while aubrites Peña Blanca and ALH 78113 came from Fornasier et al. (2008). We assumed the same albedo for the red and blue regions of JD_1 . A complete discussion of these results is provided in Section 6.2.

5. Dynamical Study

Pairing the spectroscopic analysis from Section 4 with a dynamical study would provide constraints on JD_1 ’s origin and possible connection to a parent body. We used the near-Earth object (NEO) dynamical model of Granvik et al. (2018) to calculate where JD_1 came from based on its current eccentricity, inclination, and semimajor axis of 0.222, $19^\circ.139$, and 1.216 au, respectively.

According to the Granvik et al. (2018) model, which takes into account high-inclination orbits, JD_1 has an $84\% \pm 2.1\%$ probability of coming from the ν_6 secular resonance or other resonances close by, an $11\% \pm 1.2\%$ chance of coming from the 3:1 mean-motion resonance (MMR) with Jupiter or other resonances close by, a $5\% \pm 0.8\%$ chance of coming from the Hungaria group, and a $0.4\% \pm 0.1\%$ chance of coming from the Phocaea group. Based on these probabilities, the most likely sources of origin of JD_1 would be regions in the asteroid belt feeding the ν_6 or 3:1 complex.

In Section 4, we presented a compositional connection between JD_1 and E[III] types or Angelina-like bodies. The orbit of (64) Angelina (e, i, a) = (0.125, $1^\circ.309$, 2.68 au) does not appear to agree with JD_1 ’s high orbital inclination. However, the relatively low semimajor axis of JD_1 suggests that it has spent a relatively long time in the NEO region and therefore also endured a nonnegligible number of close planetary encounters. These planetary encounters may have changed JD_1 ’s inclination dramatically. Hence, while (64) Angelina has not been linked as a possible parental body of E-type asteroids, we find it plausible that JD_1 may be genetically related to (64) Angelina and have entered the NEO region through the 3:1 MMR. Given its small size and hence rapid drift in semimajor

axis caused by the Yarkovsky effect, it may also be possible that JD_1 has moved across the 3:1 MMR rapidly enough not to be ejected from the asteroid belt and has only been ejected when it reached the ν_6 resonance (see Figure 17 in Granvik et al. 2017).

On the other hand, (434) Hungaria (e, i, a) = (0.073, $22^\circ.509$, 1.94 au) has similar orbital parameters to that of JD_1 , and the dynamical model suggests a 5% probability of coming from the Hungaria group. However, the compositional analysis of JD_1 does not agree with an origin in the Hungaria group as well as it does for Angelina-like bodies (see Section 4.2).

Dynamical considerations suggest that both the ν_6 and 3:1 resonance complexes are potential escape routes for JD_1 . Assessing whether JD_1 reached the ν_6 or 3:1 resonance complexes after being ejected from an E-type family member (i.e., the Hungaria family or a non-Hungaria family) requires extensive dynamical modeling, so we leave it for future work. We do suggest, from compositional evidence, that JD_1 falls within the Angelina-like group (Clark et al. 2004), given the strong evidence for sulfide on its surface, which is not detected in the spectra of (434) Hungaria.

6. Discussion

6.1. CPR and Radar Albedo

The SC/OC ratio, or CPR, has commonly been used as a single-parameter study for surface composition and near-surface roughness (Ostro 1993; Benner et al. 2008). Radar scattering modeling has manifest the nonlinear behavior of SC/OC ratios with composition and surface roughness mainly due to variable near-surface electric properties among different taxonomies (Virkki & Muinonen 2016). Although attempts from both observational and modeling approaches have intended to understand the behavior of the radar scattering properties of asteroid surfaces with respect their composition and particle size distribution, the area remains substantially unexplored and inconclusive. Future laboratory and modeling work would help to pivot our understanding regarding the

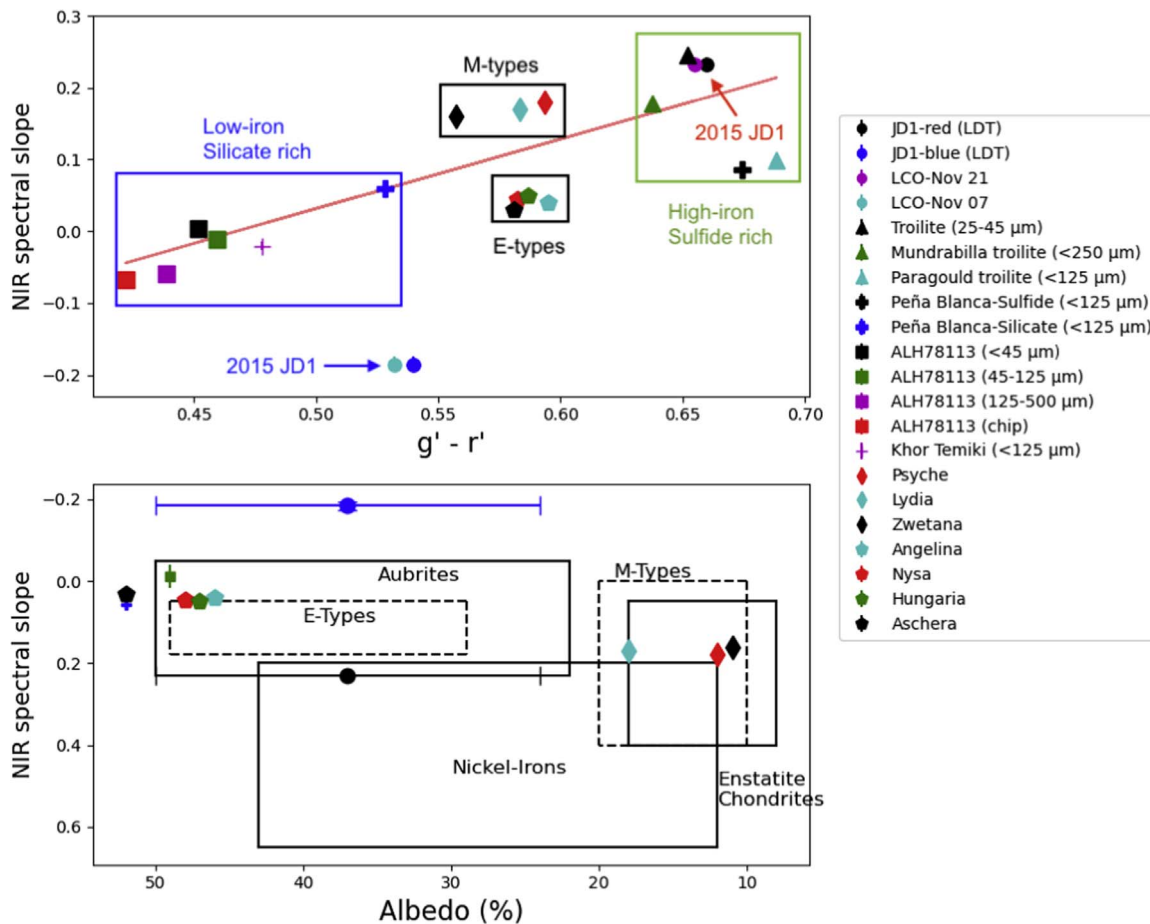


Figure 13. The NIR spectral slope as a function of the $g' - r'$ Sloan colors (top panel) and geometric albedo (bottom panel) of JD₁ (filled circles), E-types (pentagons), M-types (diamonds), ALH 78113 (squares), Peña Blanca aubrites (thick plus signs), Khor Temiki aubrites (thin plus signs), and minerals (triangles). The red line represents a linear relationship between NIR spectral slope (s') and Sloan $g' - r'$ color given by $s' = (g' - r') * (0.969 \pm 0.291) - 0.453$.

SC/OC ratio, including the identification of near-surface elements controlling radar scattering properties.

Benner et al. (2008) published average CPR values for NEAs ranging from 0.143 ± 0.055 for M-type asteroids to 0.892 ± 0.079 for E-type asteroids. Recently, Aponte-Hernandez et al. (2020) also found similar trends among taxonomic classes. Aponte-Hernandez et al. (2020) found that asteroids with $CPR > 0.75$ can be statistically, within 2σ , characterized as E-types. The E-types have presented robust statistical consistency on high CPR values (Benner et al. 2008; Busch et al. 2008; Reddy et al. 2012a; Aponte-Hernandez et al. 2020). Such a tendency might be illustrating the characteristic properties of their mineralogical composition and surface properties. Based on this CPR review, we argue that JD₁'s composition should be similar to those E-types asteroids (see Figure 14). Although no spacecraft has visited an E-type asteroid to do a direct comparison with JD₁, valuable information can be extracted from other spacecraft-visited asteroids that have radar observations. Comparatively, the CPR value of JD₁ exceeds all of those CPRs of spacecraft-visited asteroids, including S- and C-complex: (433) Eros (0.28 ± 0.06 ; Magri et al. 2001), (25143) Itokawa (0.26 ± 0.04 ; Ostro et al. 2004), (4179) Toutatis (0.23 ± 0.03 ; Magri et al. 2001), and (101955) Bennu (0.18 ± 0.03 ; Nolan et al. 2013). Given the uniqueness of the

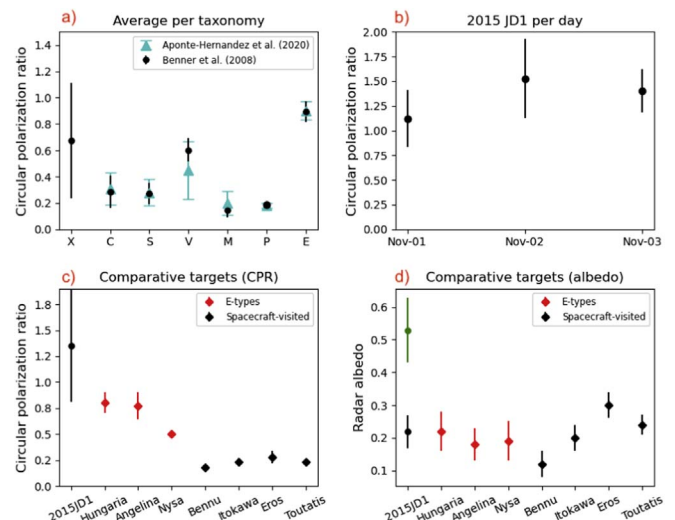


Figure 14. (a) CPRs from Benner et al. (2008) and Aponte-Hernandez et al. (2020) as a function of the Bus-DeMeo taxonomy (DeMeo et al. 2009). (b) CPRs of JD₁ as a function of observing days. (c) CPRs of JD₁ (black dot), selected E-types (red filled diamonds), and spacecraft-visited NEAs (black filled diamonds). (d) Comparative radar albedos for the asteroids in panel (c). The black and green circles correspond to the OC and total radar albedo of JD₁, respectively.

JD₁ scattering properties and lack of interpretation of such high CPR values, it is not possible to make connections with those spacecraft-observed asteroids' (i.e., Bennu, Lauretta et al. 2019; Toutatis, Jiang et al. 2015; Eros, Robinson et al. 2002; and Itokawa, Susorney et al. 2019) surface properties.

Radar albedo can be used to infer the surface properties (i.e., metallicity and density) of asteroids (Shepard et al. 2008a, 2010). From radar data compilation (Neese et al. 2012), the average $\hat{\sigma}_T$ of asteroids is $15.7\% \pm 11.1\%$ (including NEAs and main belt asteroids). The total power (SC + OC = $\hat{\sigma}_T$) of the radar-observed E-type asteroids ranges from 0.18 to 0.42 (i.e., (64) Angelina, Shepard et al. 2011; (434) Hungaria, Shepard et al. 2008b; (44) Nysa, Shepard et al. 2008b; and 1998 WT₂₄, Busch et al. 2008), while the total power of the M-type (16) Psyche (Shepard et al. 2017) ranges from 0.24 to 0.32. In addition, the total power of the spacecraft-visited asteroids shown in Figure 14(d) ranges from 0.12 to 0.3. Comparatively, JD₁'s total power ($\hat{\sigma}_T = 0.53 \pm 0.10$) radar albedo exceeds all those reported for E-types. Moreover, JD₁'s OC radar albedo is indistinguishable from the selected comparative objects but higher than Bennu's total power. Bennu has a radar albedo of 0.12 and a bulk density of 1.19 g cm^{-3} (Lauretta et al. 2019), and comets have typical radar albedos ranging from 0.4 to 0.1 and densities below 1 g cm^{-3} (Harmon et al. 1999, 2004, 2011); thus, we can reject a low near-surface density for JD₁.

The comparison between JD₁'s disk-integrated radar albedo and those of E- and M-types suggests some metal content near the surface. Adopting the Shepard et al. (2010) relationship, we obtained an approximate upper-limit density of 2.5 g cm^{-3} for a 30% porosity using typical aubrite grain densities of 3.5 g cm^{-3} from Britt & Consolmagno (2003).

6.2. Compositional Analysis of the Surface

Figure 13 (top panel) has four boxes indicating regions with either similar compositions or similar taxonomies; i.e., black boxes indicate E- and M-types, the green box shows meteorites and minerals rich in iron and sulfide, and the blue box indicates meteorites rich in enstatite silicate with low iron abundances. The first fact to notice is the mineralogical composition effect. This analysis shows that meteorites with higher iron and sulfide abundances have redder spectral slopes and $g' - r'$ colors, while bluer colors and spectral slopes are observed for meteorites whose mineralogical composition is shown to be richer in enstatite silicates and lower in iron. The M-types have steeper spectral slopes than E-types due to the higher iron content, which can also be observed in our sample of well-known E/M-type asteroids. Second, JD₁'s negative NIR spectral slope and blue colors deviate from the positive NIR spectral slope and red colors, suggesting that such a blue region is compositionally distinct. Object JD₁'s spectral red surface has a steeper slope and redder Sloan colors than E/M-types and is mineralogically consistent with the spectral properties of iron sulfides (i.e., the mineral troilite and Peña Blanca sulfide region). Similarly, the red NIR spectral slope of JD₁ as a function of its geometric albedo places it between the aubrites and nickel-iron regions, suggesting as well some iron composition. The spectral blue region has a bluer slope than the selected aubrites and aubrite slope ranges presented in the bottom panel. The blue Sloan colors of JD₁ are similar to those of the Peña Blanca silicate region. Such spectral similarities with aubrites ALH 78113, Peña Blanca silicate region, and Khor Temiki suggest a composition abundant in enstatite

silicate and low iron content. The blue region could still preserve some sulfide end-members, since both LCO spectra show the $0.5 \mu\text{m}$ feature.

In Figure 11 (top left panel), two spectra of the Peña Blanca meteorite are shown. The steeper reflectance (red dashed line) is from the sulfide-rich region, while the other one is from an enstatite silicate region. The NIR similarity between the JD₁ red-sloped spectra and the Peña Blanca sulfide region suggests a common mineralogical composition, while JD₁'s blue Sloan colors support a Peña Blanca silicate-like composition. Peña Blanca Spring is a fragmental breccia of particular interest because it contains large crystals of enstatite ($\sim 10 \text{ cm}$ in diameter from the largest extension), which have been attributed to an igneous formation (Lonsdale 1947). The bulk analysis of Peña Blanca Spring, which corresponds to the silicate region spectra referred to in this work, revealed a high abundance of enstatite (95 wt.%) with low iron, plagioclase (2.1 wt.%), diopside (2.7 wt.%), forsterite (0.3 wt.%), and sulfide end-members in lower abundances (0.2 wt.%; Watters & Prinz 1979; Lonsdale 1947). The chemical analysis of the Peña Blanca sulfide region mentioned here yielded a high iron abundance and an Fe/Ni of 22.68 (Lodders et al. 1993). This comparison between the Peña Blanca chemical analysis and JD₁ is in agreement with the analysis of the NIR spectral slope and Sloan colors.

Another fragmental breccia with chondritic-like inclusions is ALH 78113, similar to Cumberland Falls, with large enstatite fragments ($\sim 5 \text{ cm}$ in diameter). Based on those inclusions, Lipschutz et al. (1988) concluded that ALH 78113 is a representative of foreign primitive fragments, not necessarily formed under the same conditions as enstatite achondrite meteorites, that collided with the aubrite parent body. The bulk chemical analysis indicates that enstatite is the most abundant mineral (Kimura et al. 1993). The silicate phases show feldspar, olivine, glass, diopside, enstatite, and silica mineral (Lipschutz et al. 1988; Kimura et al. 1993). The bluest spectral slope of JD₁ is $\sim 10\%$ more negative than the bluer spectral slope of ALH 78113 (see the green spectrum with grains $>$ chip size in the left panel of Figure 12). It is likely, as indicated by the comparison with Peña Blanca and from the slope-color analysis, that the blue (spectral) region on JD₁ contains lower abundances of Fe/Ni and larger grain sizes than ALH 78113 and the rest of its surface.

6.3. Possible Explanations for the Spectral Variability

In Section 6.2, we investigate the spectral slope and color variation of JD₁. However, it is difficult to explain the nature of JD₁'s spectral variability with the available data. Therefore, we provide the following hypotheses that could yield the observed variability.

1. *Space weathering.* Several active comets are known to show longitudinal spectral variations in their surfaces in a relatively limited time frame (Luk'yanyk et al. 2019) due to the sublimation of icy grains. The NIR spectra of (6478) Gault, which is known to be an active asteroid, showed a slope variation of $22.6\% \mu\text{m}^{-1}$ (Marsset et al. 2019). They hypothesized that the NIR spectral variation was likely due to a loss of regolith, resulting in the exposure of newer material. As mentioned in Section 5, the low semimajor axis of JD₁ suggests a considerable number of close planetary encounters. It could be

possible that these planetary encounters played a role in resurfacing the body (i.e., near its neck), yielding the exposure of unweathered or fresher (bluer) material.

2. *Accretion.* Object JD₁ could have been formed through the accretion of heterogeneous fragments. This could be a case where the parent body of JD₁ was disrupted by a compositionally different impactor, or the progenitor itself possessed heterogeneity.
3. *Exogenous material.* The recently spacecraft-visited asteroids Ryugu and Bennu revealed bright boulders spectrally distinct from the dark ones on their surfaces. Recent studies suggest that such bright boulders represent remnants of exogenous compositionally different material (DellaGiustina et al. 2021; Tatsumi et al. 2021). In the case of JD₁, partial surface blanketing by exogenous material could have created a spectrally blue surface “patch” covering a notable portion of its surface. In addition, our compositional analysis shows spectral similarities between JD₁’s blue spectra and the aubrite ALH 781113. Lipschutz et al. (1988) suggested that ALH 78113 could have been a surviving fragment from an external igneous body that collided with the E-type progenitor(s). Furthermore, the exogenous material on Bennu and Ryugu made up a tiny fraction of their surfaces (<0.1%). While the likelihood of having a significant portion of JD₁’s surface contaminated by exogenous material seems very low, this hypothesis may still be plausible.

7. Conclusions

Through the combination of ground-based telescopic observations covering the visible, NIR, and radar wavelengths, we physically characterized the NEA 2015 JD₁, finding interesting and possibly unique surface features of this small airless body. In summary, we found that JD₁ has a contact binary nature with a head of ~ 50 m and a body of ~ 100 m across the longest visible axis projection, or approximately between 150 and 190 m in diameter. It has a high CPR, between 1.12 and 1.52, one of the highest values measured for NEAs, as well as a high total radar albedo of 0.53 ± 0.01 . We measured a high geometric albedo of 0.35 ± 0.12 that is consistent with an E-type taxonomy (Thomas et al. 2011). We derived a $g' - r'$ color of 0.6 ± 0.03 . Our dynamical study suggests that both the ν_6 and 3:1 resonance complexes are potential escape routes for JD₁. Spectral comparison suggests a compositional link between JD₁ and the Angelina-like group from Clark et al. (2004).

Our rotationally resolved spectroscopy revealed red and blue NIR spectra on the surface of JD₁. Our comprehensive analysis of the observed rotational spectral variability allows us to draw the following conclusion: JD₁ is likely an E-type asteroid rich in sulfides and iron with a portion of its surface that could consist of larger grain sizes and/or be mineralogically richer in silicates and deficient in iron, responsible for the spectral variability observed. Object JD₁ could be one of the first subkilometer NEAs to show spectral variability likely associated with a heterogeneous composition and grain sizes.

We plan to continue this investigation in order to validate the spectral heterogeneity on the surface of JD₁ using spectrophotometry and spectroscopy observations. The next close approach of JD₁ will take place around 2023 April with a

predicted V-band magnitude of 19.8. The next radar apparition at a comparable distance to that in 2019 (0.034 au) will occur near 2058 November, when JD₁ is expected to have a V magnitude of 15.1.

This work was supported in part by the Arizona Board of Regents, Arizona’s Technology and Research Initiative Fund, and NASA grant No. NNX15AF81G to D.E.T. These results made use of the Lowell Discovery Telescope (LDT) at Lowell Observatory. The LDT is localized on homelands sacred to Native Americans. We thank them for allowing part of their sacred lands to be used for astronomical research. Lowell is a private, nonprofit institution dedicated to astrophysical research and public appreciation of astronomy and operates the LDT in partnership with Boston University, the University of Maryland, the University of Toledo, Northern Arizona University, and Yale University.

The Near-Infrared High Throughput Spectrograph was funded by NASA award No. NNX09AB54G through its Planetary Astronomy and Planetary Major Equipment programs. The Large Monolithic Imager was built by Lowell Observatory using funds provided by the National Science Foundation (AST-1005313).

Part of this work was done at the Arecibo Observatory, which is a facility of the National Science Foundation operated under cooperative agreement by the University of Central Florida, Yang Enterprises, Inc., and Universidad Metropolitana. The Arecibo Planetary Radar Program is supported by NASA grants 80NSSC19K0523 and NNX13AQ46G through the Near-Earth Object Observations program.

This material is supported in part by the National Science Foundation Graduate Research Fellowship Program under grants No. 2021318193 to A.J.L.O. and No. 2018258765 to C.O.C. Any opinions, findings, and conclusions or recommendations expressed in this material are those of the author(s) and do not necessarily reflect the views of the National Science Foundation.


Parts of the computational analyses were carried out on Northern Arizona University’s Monsoon computing cluster, funded by Arizona’s Technology and Research Initiative Fund. This research has made use of data and/or services provided by the International Astronomical Union’s Minor Planet Center. This research has made use of NASA’s Astrophysics Data System. This research has made use of the SkyBoT Virtual Observatory tool (Berthier et al. 2006).

Facility: Arecibo, Lowell Discovery Telescope, Las Cumbres Observatory.


Software: *Spextool* (Cushing et al. 2004), *Astropy* (Astropy Collaboration et al. 2013), *Scipy* (Virtanen et al. 2020), *Numpy* (van der Walt et al. 2011; Harris et al. 2020), *Matplotlib* (Hunter 2007), Photometry Pipeline (Mommert 2017), *SEXtractor* (Bertin & Arnouts 1996), *SCAMP* (Bertin 2006), *SAO Image DS9* (Joye & Mandel 2003), *Aperture Photometry Tool* (Laher et al. 2012), *Horizons System*.¹³

ORCID iDs

Andy López-Oquendo  <https://orcid.org/0000-0002-2601-6954>

David E. Trilling  <https://orcid.org/0000-0003-4580-3790>

Annika Gustafsson  <https://orcid.org/0000-0002-7600-4652>

Anne Virkki  <https://orcid.org/0000-0002-4129-5381>

¹³ <https://ssd.jpl.nasa.gov/horizons/app.html>

Edgard G. Rivera-Valentín  <https://orcid.org/0000-0002-4042-003X>

Mikael Granvik  <https://orcid.org/0000-0002-5624-1888>

Colin Orion Chandler  <https://orcid.org/0000-0001-7335-1715>

Joseph Chatelain  <https://orcid.org/0000-0002-1278-5998>

Patrick Taylor  <https://orcid.org/0000-0002-2493-943X>

Luisa Fernanda-Zambrano  <https://orcid.org/0000-0002-6615-4040>

References

- Ahn, C. P., Alexandro, R., Allende Prieto, C., et al. 2012, *ApJS*, 203, 21
- Aponte-Hernandez, B., Rivera-Valentín, E. G., & Taylor, P. A. 2020, *LPSC*, 52, 2940
- Astropy Collaboration, Robitaille, T. P., Tollerud, E. J., et al. 2013, *A&A*, 558, A33
- Bell, J. F., Owensby, P. D., Hawke, B. R., & Gaffey, M. J. 1988, *LPSC*, 19, 57
- Benner, L. A., Ostro, S. J., Magri, C., et al. 2008, *Icar*, 198, 294
- Berthier, J., Vachier, F., Thuillot, W., et al. 2006, in ASP Conf. Ser. 351, *SkyBoT*, a New VO Service to Identify Solar System Objects, ed. C. Gabriel et al. (San Francisco, CA: ASP), 367
- Bertin, E. 2006, in ASP Conf. Ser. 351, *Astronomical Data Analysis Software and Systems XV*, ed. C. Gabriel et al. (San Francisco, CA: ASP), 112
- Bertin, E., & Arnouts, S. 1996, *A&AS*, 117, 393
- Binzel, R. P., DeMeo, F. E., Turtelboom, E. V., et al. 2019, *Icar*, 324, 41
- Binzel, R. P., Harris, A. W., Bus, S. J., & Burbine, T. H. 2001, *Icar*, 151, 139
- Botke, W. F., Morbidelli, A., Jedicke, R., et al. 2002, *Icar*, 156, 399
- Bowell, E., Hapke, B., Domingue, D., et al. 1989, in *Asteroids II*, ed. R. P. Binzel, T. Gehrels, & M. S. Matthews (Tucson, AZ: Univ. Arizona Press), 524
- Britt, D. T., & Consolmagno, G. J. 2003, *M&PS*, 38, 1161
- Bus, S. J., & Binzel, R. P. 2002, *Icar*, 158, 106
- Busch, M. W., Benner, L. A. M., Ostro, S. J., et al. 2008, *Icar*, 195, 614
- Castro, P., Payne, T., Moody, J., et al. 2018, in *The Advanced Maui Optical and Space Surveillance Technologies Conf.*, ed. S. Ryan (Maui, HI: AMOS), 36
- Chambers, K. C., Magnier, E. A., Metcalfe, N., et al. 2016, arXiv:1612.05560
- Clark, B. E., Bus, S. J., Rivkin, A. S., et al. 2004, *JGRE*, 109, E02001
- Cloutis, E. A., Gaffey, M. J., Smith, D. G. W., & Lambert, R. S. J. 1990, *JGR*, 95, 8323
- Cushing, M. C., Vacca, W. D., & Rayner, J. T. 2004, *PASP*, 116, 362
- DellaGiustina, D. N., Kaplan, H. H., Simon, A. A., et al. 2021, *NatAs*, 5, 31
- DeMeo, F. E., Binzel, R. P., Slivan, S. M., & Bus, S. J. 2009, *Icar*, 202, 160
- DeMeo, F. E., & Carry, B. 2014, *Natur*, 505, 629
- Devogèle, M., Ferrais, M., Jehin, E., et al. 2021, *MNRAS*, 505, 245
- Devogèle, M., Tanga, P., Cellino, A., et al. 2018, *Icar*, 304, 31
- Doi, M., Tanaka, M., Fukugita, M., et al. 2010, *AJ*, 139, 1628
- Dunham, E. W., Bida, T. A., Chylek, T., et al. 2018, *Proc. SPIE*, 10702, 1094
- Fornasier, S., Migliorini, A., Dotto, E., & Barucci, M. A. 2008, *Icar*, 196, 119
- Fowler, J. W., & Chillemi, J. R. 1992, *The IRAS Minor Planet Survey*, 17 (Hanscom AF Base, MA: Phillips Laboratory), 43
- Gaffey, M. J. 1976, *JGR*, 81, 905
- Gaffey, M. J. 1983, 14th *LPSC*, 497, 14
- Gaffey, M. J., & Kelley, M. S. 2004, *LPSC*, 35, 1812
- Gaia Collaboration, Prusti, T., de Bruijne, J. H. J., et al. 2016, *A&A*, 595, A1
- Granvik, M., Morbidelli, A., Jedicke, R., et al. 2018, *Icar*, 312, 181
- Granvik, M., Morbidelli, A., Vokrouhlický, D., et al. 2017, *A&A*, 598, A52
- Gunn, J. E., Carr, M., Rockosi, C., et al. 1998, *AJ*, 116, 3040
- Gustafsson, A., Moskovitz, N., Cushing, M. C., et al. 2021, *PASP*, 133, 035001
- Harmon, J. K., Campbell, D. B., Ostro, S. J., & Nolan, M. C. 1999, *P&SS*, 47, 1409
- Harmon, J. K., Nolan, M. C., Howell, E. S., Giorgini, J. D., & Taylor, P. A. 2011, *ApJL*, 734, L2
- Harmon, J. K., Nolan, M. C., Ostro, S. J., & Campbell, D. B. 2004, in *Comets II*, ed. M. C. Festou, H. U. Keller, & H. A. Weaver (Tucson, AZ: Univ. Arizona Press), 265
- Harris, C. R., Millman, K. J., van der Walt, S. J., et al. 2020, *Natur*, 585, 357
- Hunter, J. D. 2007, *CSE*, 9, 90
- Jedicke, R., Granvik, M., Micheli, M., et al. 2015, in *Asteroids IV*, ed. P. Michel, F. E. DeMeo, & W. F. Botke (Tucson, AZ: Univ. Arizona Press), 795
- Jiang, Y., Ji, J., Huang, J., et al. 2015, *NatSR*, 5, 16029
- Joye, W. A., & Mandel, E. 2003, in ASP Conf. Ser. 295, *New Features of SAOImage DS9*, ed. H. E. Payne, R. I. Jedrzejewski, & R. N. Hook (San Francisco, CA: ASP), 489
- Keil, K. 2010, *ChEG*, 70, 295
- Kimura, M., Lin, Y.-T., Ikeda, Y., et al. 1993, *AMR*, 6, 186
- Laher, R. R., Gorjian, V., Rebull, L. M., et al. 2012, *PASP*, 124, 737
- Larson, S., Brownlee, J., Hergenrother, C., & Spahr, T. 1998, *BAAS*, 30, 1037
- Lauretta, D. S., Dellagiustina, D. N., Bennett, C. A., et al. 2019, *Natur*, 568, 55
- Lazzarin, M., Petropoulou, V., Bertini, I., et al. 2019, *P&SS*, 165, 115
- Lipschutz, M. E., Verkouteren, R. M., Sears, D. W. G., et al. 1988, *GeCoA*, 52, 1835
- Lister, T. A., Gomez, E., Chatelain, J., et al. 2021, *Icar*, 364, 114387
- Lodders, K., Palme, H., & Wlotzka, F. 1993, *Metic*, 28, 538
- Lonsdale, J. 1947, *AmMin*, 32, 354, <https://pubs.geoscienceworld.org/msa/ammin/article-pdf/32/5-6/354/4243845/am-1947-354.pdf>
- Luk'yanyk, I., Zubko, E., Husárik, M., et al. 2019, *MNRAS*, 485, 4013
- Magri, C., Consolmagno, G. J., Ostro, S. J., Benner, L. A. M., & Beeny, B. R. 2001, *M&PS*, 36, 1697
- Mainzer, A., Grav, T., Bauer, J., et al. 2011, *ApJ*, 743, 156
- Marsset, M., DeMeo, F., Sonka, A., et al. 2019, *ApJL*, 882, L2
- Masiero, J. R., Grav, T., Mainzer, A. K., et al. 2014, *ApJ*, 791, 121
- Masiero, J. R., Wright, E. L., & Mainzer, A. K. 2021, *PSJ*, 2, 32
- Massey, P., Dunham, E. W., Bida, T. A., et al. 2013, *AAS Meeting*, 221, 345.02
- Mommert, M. 2017, *A&C*, 18, 47
- Naidu, S., Benner, L., Brozovic, M., et al. 2020, *Icar*, 348, 113777
- Nathues, A. 2010, *Icar*, 208, 252
- Neese, C., Benner, L. A. M., & Ostro, S. J. 2012, *NASA Planetary Data System*, *EAR-A-5-DDR-RADAR-V18.0*
- Nolan, M. C., Magri, C., Howell, E. S., et al. 2013, *Icar*, 226, 629
- Ochsenbein, F., Bauer, P., & Marcout, J. 2000, *A&AS*, 143, 23
- Ostro, S. J. 1993, *RvMP*, 65, 1235
- Ostro, S. J., Benner, L. A. M., Nolan, M. C., et al. 2004, *M&PS*, 39, 407
- Perna, D., Barucci, M. A., Fulchignoni, M., et al. 2018, *P&SS*, 157, 82
- Rabinowitz, D. L. 1991, *AJ*, 101, 1518
- Reddy, V., Nathues, A., Le Corre, L., et al. 2012a, *Sci*, 336, 700
- Reddy, V., Sanchez, J. A., Nathues, A., et al. 2012b, *Icar*, 217, 153
- Robinson, M. S., Thomas, P. C., Veverka, J., Murchie, S. L., & Wilcox, B. B. 2002, *M&PS*, 37, 1651
- Russell, C. T., Raymond, C. A., Coradini, A., et al. 2012, *Sci*, 336, 684
- Sanchez, J. A., Reddy, V., Nathues, A., et al. 2012, *Icar*, 220, 36
- Sanchez, J. A., Reddy, V., Shepard, M. K., et al. 2017, *AJ*, 153, 29
- Shepard, M. K., Clark, B. E., Nolan, M. C., et al. 2008a, *Icar*, 195, 184
- Shepard, M. K., Clark, B. E., Ockert-Bell, M., et al. 2010, *Icar*, 208, 221
- Shepard, M. K., Harris, A. W., Taylor, P. A., et al. 2011, *Icar*, 215, 547
- Shepard, M. K., Kressler, K. M., Clark, B. E., et al. 2008b, *Icar*, 195, 220
- Shepard, M. K., Richardson, J., Taylor, P. A., et al. 2017, *Icar*, 281, 388
- Stokes, G. H., Evans, J. B., Vighh, H. E. M., Shelly, F. C., & Pearce, E. C. 2000, *Icar*, 148, 21
- Sugimoto, C., Tatsumi, E., Cho, Y., et al. 2021, *Icar*, 369, 114591
- Susorney, H. C. M., Johnson, C. L., Barnouin, O. S., et al. 2019, *Icar*, 325, 141
- Ivezić, Ž., Tabachnik, S., Rafikov, R., et al. 2001, *AJ*, 122, 2749
- Tatsumi, E., Sugimoto, C., Riu, L., et al. 2021, *NatAs*, 5, 39
- Taylor, P. A., Rivera-Valentín, E. G., Benner, L. A. M., et al. 2019, *P&SS*, 167, 1
- Tedesco, E. F. 2005, *NASA Planetary Data System*, *EAR-A-5-DDR-UBV-MEAN-VALUES-V1.2*
- Thomas, C. A., Trilling, D. E., Emery, J. P., et al. 2011, *AJ*, 142, 85
- Trilling, D., Mommert, M., Hora, J., et al. 2016, *NEOLegacy: The ultimate Spitzer survey of Near Earth Objects*, *Spitzer Proposal ID 13006*, *NASA van der Walt, S., Colbert, S. C., & Varoquaux, G. 2011, CSE*, 13, 22
- Virkki, A., Marshall, S. E., Venditti, F. C. F., et al. 2022, *PSJ*, submitted
- Virkki, A., & Muinonen, K. 2016, *Icar*, 269, 38
- Virkki, A., Nolan, M., Taylor, P., et al. 2014, in *Asteroids, Comets, Meteors 2014*, ed. K. Muinonen et al. (Helsinki: ACM), 568
- Virtanen, P., Gommers, R., Oliphant, T. E., et al. 2020, *NatMe*, 17, 261
- Warner, B. D., & Stephens, R. D. 2020, *MPBu*, 47, 105
- Watters, T. R., & Prinz, M. 1979, *LPSC*, 10, 1319
- Willmer, C. N. A. 2018, *ApJS*, 236, 47
- Zellner, B., Leake, M., Morrison, D., & Williams, J. G. 1977, *GeCoA*, 41, 1759
- Zellner, B., Tholen, D. J., & Tedesco, E. F. 1985, *Icar*, 61, 355